Computational Materials Science 249 (2025) 113627

Contents lists available at ScienceDirect

Computational Materials Science

journal homepage: www.elsevier.com/locate/commatsci

Full length article

Solidification of a quaternary X5CrNi18-10 alloy during laser beam welding using CALPHAD data in a phase-field approach

Muhammad Umar [a,b,*], Marco Seiz [b,c,d], Michael Kellner [b], Britta Nestler [a,b,c], Daniel Schneider [a,b,c]

[a] Institute for Digital Materials Science (IDM), Karlsruhe University of Applied Sciences, Moltkestraße 30, Karlsruhe, 76133, Germany
[b] Institute for Applied Materials - Microstructure Modelling and Simulation (IAM-MMS), Karlsruhe Institute of Technology (KIT), Straße am Forum 7, Karlsruhe, 76131, Germany
[c] Institute of Nanotechnology (INT), Karlsruhe Institute of Technology (KIT), Hermann-von-Helmholtz-Platz 1, Eggenstein-Leopoldshafen, 76344, Germany
[d] Faculty of Mechanical Engineering, Kyoto Institute of Technology, Matsugasaki, Sakyo–ku, Kyoto, 606–8585, Japan

ARTICLE INFO

Keywords:
Alloy solidification
Laser beam welding
Quaternary X5CrNi18-10 alloy
CALPHAD database
Phase-field simulations
Weld quality
Dendritic microstructure
Thermochemical modelling

ABSTRACT

Dendritic growth is a common phenomenon during the solidification of alloys, and it has a significant impact on the final microstructure and mechanical properties of the material. This research study investigates the solidification behaviour of quaternary X5CrNi18-10 alloys at thermochemical conditions similar to the laser beam welding (LBW) process. The aim of this investigation is to gain a comprehensive understanding of microstructure evolution at the microscale and their correlation with the macroscopic welding process conditions. To achieve this, a combined approach using the CALculation of PHAse Diagrams (CALPHAD) database and phase-field simulations is employed. Based on the CALPHAD-derived Gibbs energy functions, phase-field simulations are performed to simulate the solidification with dendritic/cellular morphology. The study focuses on solidification microstructure evolution influenced by process conditions such as thermal gradient and LBW velocity at steady-state conditions. By analysing the solidification microstructure morphology in 2D, valuable insights into the solidification kinetics and the influence of local thermal conditions on dendritic growth are obtained. Furthermore, the micro-segregation behaviour of key alloying elements during solidification in the mushy zone is explored. This study will help to enhance the understanding of dendritic solidification in this welding process, facilitating the optimisation of process parameters for improved mechanical properties.

1. Introduction

Dendrite growth can be influenced by various factors, including alloy composition, cooling rate and solidification conditions [1,2]. During dendritic solidification, the inhomogeneous distribution of alloying elements can have a significant effect on the microstructure and the mechanical properties of the resulting material [3]. In the case of dendritic solidification, microsegregation can be particularly pronounced, due to the complex growth patterns of the dendrites [4]. The solute atoms can be trapped in the dendrite arms, swept by the solidifying interface, resulting in a concentration gradient of solutes in the microstructure. A particular manifestation of the detrimental influence of a highly segregated microstructure can be observed, for example, during the solidification of the weld pool after laser beam welding (LBW) of X5CrNi18-10 alloy [5]. The concentration gradient of the solute leads to a chemically inhomogeneous microstructure at the final stage of solidification. This chemical inhomogeneity can cause the formation of low-melting point phases in interdendritic areas or local changes in solidification temperature ranges, potentially causing residual liquid films to persist at grain boundaries. In-homogeneous solidification can lead to differential thermal contraction, generating residual stresses that may contribute to crack initiation and propagation [6]. Segregation of certain elements (e.g., carbon and nickel) to grain boundaries can significantly reduce ductility, making the material more susceptible to cracking under solidification stresses [7]. The multi-directional dendrite arms form a network of morphologically complex solids in which various points act as stress concentrators [8–10]. Even before the solid-state phase transformation to $\gamma - Fe$ takes place, these points can no longer withstand the stresses due to further cooling and are subjected to considerable mechanical stresses, resulting in microcracks [11–13]. These microcracks can lead to hot longitudinal cracks along the centre

* Corresponding author at: Institute for Digital Materials Science (IDM), Karlsruhe University of Applied Sciences, Moltkestraße 30, Karlsruhe, 76133, Germany.
E-mail address: muhammad.umar@partner.kit.edu (M. Umar).

https://doi.org/10.1016/j.commatsci.2024.113627
Received 14 September 2024; Received in revised form 18 December 2024; Accepted 18 December 2024
Available online 8 January 2025

line of weld seam [14]. Although the solidification cracking problem has been studied by many researchers yet there exists a need of finding correct and well-understood relationship of LBW process parameters with local dendritic morphology and microsegregation behaviour.

The phase-field method is a useful computational tool for simulating the solidification of alloys. In the phase-field method, interfaces are not explicitly tracked. Instead, they are represented as gradual transitions over a finite region, typically through a smooth function. This continuous representation enables a more natural and efficient handling of complex interface geometries and topological changes, using a diffuse interface. The combination of CALPHAD-based thermodynamic modelling and phase-field simulations enable investigating solidification phenomena in complex alloy systems. Experimental studies such as [15–18] have made important observations which have contributed to the understanding of the basic mechanisms of dendritic solidification. Additionally, the phase-field method first developed for dendritic solidification and used by Kobayashi et al. [19] revealed the computational possibility of modelling such a complex system of patterns. Warren et al. [20] developed a computational model of isothermal dendritic solidification for a binary alloy and presented a redistribution pattern of solutes with secondary and tertiary side arms. They presented the results of a phase-field simulation with a limited resolution of a simpler system, due to the scarce computational resources available at that time. Later, numerous studies on the solidification behaviour of alloys were carried out with the aid of phase-field simulations [19,21–24]. It was found that microsegregation is strongly influenced by the interfacial energy anisotropy, undercooling at the solid–liquid interface and the solute segregation coefficient. These local chemical inhomogeneities lead to fluctuations in mechanical strength and sometimes to solidification cracks, usually along the centre line of the weld. The relationship between the processing parameters during LBW and the microstructure of stainless steel is complex and a thorough understanding of these interactions is still required to optimise the microstructure and properties of these materials. Investigations are required to characterise the influence of various factors on dendrite growth in stainless steels and to develop strategies to control the dendrite morphology. Therefore, there is an urgent need to understand the problem in thermochemical environments with high temperature gradients and welding speeds in industrially relevant, time-efficient processes such as LBW.

A quantitative determination of the temperature-dependent Gibbs free energy in a multiphase multi-component (Fe–C–Cr–Ni) alloy system is crucial to get quantitative accuracy from phase-field simulations. The driving force is dictated by these functions for phase composition, solute rejection, and chemical driving forces for solidification. Although the CALPHAD methodology has emerged as a robust tool for thermodynamic coupling with phase-field simulations, but the computational expense of directly coupling with a CALPHAD database [25] is high due to the complex formulation of Gibbs energy functions given by the general expression as:

$$\Delta G_{mol} = \Delta G_{mol}^{ideal} + \Delta G_{mol}^{mech} + \Delta G_{mol}^{excess}, \tag{1}$$

where ΔG_{mol} is the molar Gibbs energy of the alloy system. It is calculated by adding Gibbs energy contribution due to mechanical mixing of species i.e., ΔG_{mol}^{mech} and the excess energy i.e., ΔG_{mol}^{excess} to the Gibbs energy of alloy as per ideal solution model i.e., ΔG_{mol}^{ideal}. The complexity increases drastically when the number of alloy elements in the system is increased. To reduce this complexity, an efficient and easy-to-use parabolic fitting method was recently reported by Dargahi et al. [26] to fit the Gibbs energy functions near the thermodynamical point of interest i.e., in a particular temperature and composition range. The number of Central Processing Unit (CPU) cycles required to calculate a single point in the simulation domain with full function coupling of the CALPHAD database is almost ten times higher compared to locally approximated Gibbs energy functions for a quaternary alloy [26]. The reason for this computational efficiency is that the calculation of the regular and subregular solution models with several expressions is replaced by a comparatively simple parabolic function. To leverage the grand-potential-based phase-field model introduced by Choudhury et al. [27] and Plapp [28] for simplified interface equilibrium conditions, these parabolic Gibbs energy functions are easily invertible and provide sufficient differentiability. The parabolic fitting method with reduced calculation times has already been described in various calculation studies for binary and ternary alloy systems [29–32]. There is still a gap to extend this technique for a quaternary system and to address the corresponding challenges and their potential solutions. In this study, the methodology for fitting Gibbs energy functions for a quaternary alloy system is developed and applied on Fe–C–Cr–Ni alloy system with high accuracy. Phase-field simulations for multi-component alloy with multi-phase system are performed for conditions relevant to the LBW process to see the microstructure evolution under various local thermal conditions. The dendritic/cellular morphologies with respective quantitative segregation of alloy elements is investigated and its correlation with the local heterogeneity is highlighted.

The phase-field method with Gibbs energy functions based on CALPHAD database is used according to the method described in Section 2. This section also describes the details of the governing equations of the multiphase and multi-component phase-field model based on the grand-potential. In Section 4, the results of the simulation study on the morphology and microsegregation behaviour during solidification of the quaternary alloy X5CrNi18-10, at different cooling rates are described. Discussion of the results in context of the scientific state of the art is presented in Section 5, followed by the conclusions of this simulation study summarised in Section 6.

2. Material and methods

For modelling the solidification behaviour, the scope of this work is focused on the two-phase region in terms of temperature range, i.e., 1730 K<T<1749 K. An isotherm in Fig. 1 (A) calculated using Thermo-calc [33] shows the two phase region of interest with a little intersection sign where tie lines from Cr (20.28 at %) and Ni (9.07 at %) meet. During solidification, this material undergoes a monotectic phase transformation and forms a solid phase, referred to as $\delta-$Fe, with liquid phase which has different concentrations from the original liquid and is referred to as *Liq* in the pseudo-binary phase diagram in Fig. 1 (B). The extreme solidification conditions that normally prevail during LBW often lead to high cooling rates and thus to higher solidification driving forces. The interface of the solidifying material becomes unstable due to local thermochemical conditions, and a columnar dendritic structure is usually observed. This complicated microstructure is studied by taking into account the local thermal conditions with phase-field simulations based on the following mathematical model.

2.1. Mathematical model

The grand-potential-based multiphase multi-component phase-field model used in this study is derived from the grand potential of the system $\Omega(T, \boldsymbol{\mu}, \boldsymbol{\phi})$ depending on the temperature T, the chemical potential $\boldsymbol{\mu}$, and the phase-field variable $\boldsymbol{\phi}$ [28,35], reading as:

$$\Omega(T, \boldsymbol{\mu}, \boldsymbol{\phi}) = \int_{\Omega} \left[\Psi(T, \mu, \boldsymbol{\phi}) + \left(\epsilon a(\boldsymbol{\phi}, \nabla\boldsymbol{\phi}) + \frac{1}{\epsilon}\omega(\boldsymbol{\phi}) \right) \right] \mathrm{d}\Omega, \tag{2}$$

$$\boldsymbol{\Psi}(T, \boldsymbol{\mu}, \boldsymbol{\phi}) = \sum_{\alpha=1}^{N} \Psi_{\alpha}(T, \boldsymbol{\mu})\, h(\boldsymbol{\phi}_{\alpha}), \tag{3}$$

$$\Psi_{\alpha}(T, \boldsymbol{\mu}) = G_{\alpha}\left(\mathbf{c}_{\alpha}(T, \boldsymbol{\mu}), T\right) - \sum_{i=1}^{K-1} \mu_i \cdot c_i^{\alpha}(T, \boldsymbol{\mu}). \tag{4}$$

The grand-potential of the system over the domain Ω represents the total driving force in the bulk, which is written using the interpolation function $h(\boldsymbol{\phi}_{\alpha})$ defined as:

$$h(\boldsymbol{\phi}_{\alpha}) = \boldsymbol{\phi}_{\alpha}^{2}(3 - 2\boldsymbol{\phi}_{\alpha}). \tag{5}$$

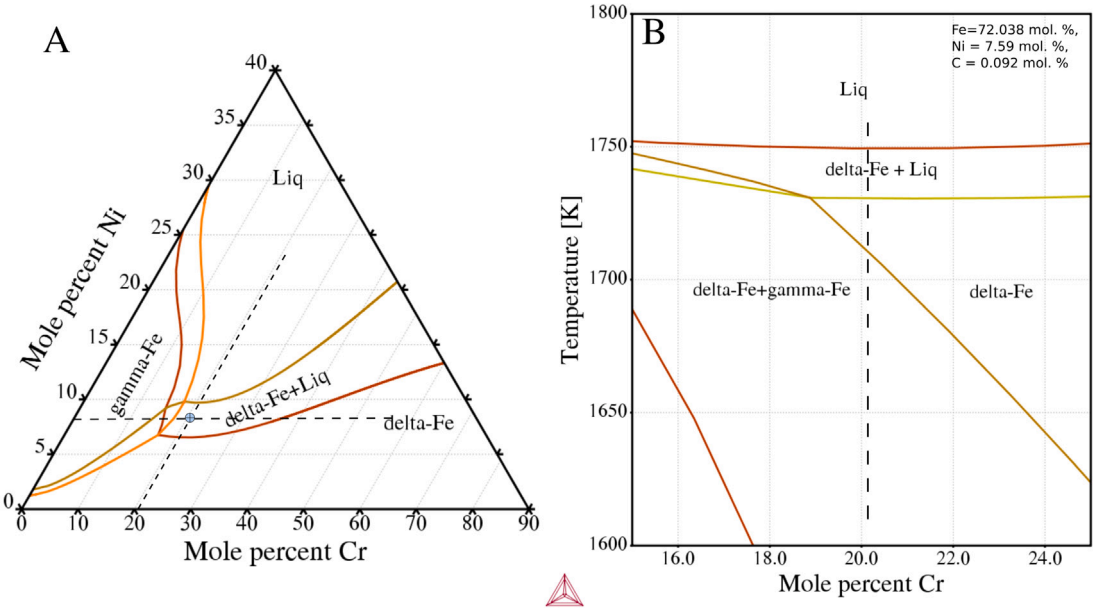

Fig. 1. Thermodynamic equilibrium phase diagrams of a quaternary (Fe–C–Cr–Ni) alloy from CALPHAD database [34], (A) a pseudo-ternary phase diagram at 1738 K where the point of interest is shown with the cross-section of tie lines and (B) a pseudo-binary phase diagram showing a dashed line corresponding to the concentration of chromium in the alloy.

The parameter ϵ is related to the numerical interface thickness while the interface contribution to the functional is given by the terms $a(\boldsymbol{\phi}, \nabla\boldsymbol{\phi})$ and $\omega(\boldsymbol{\phi})$ as gradient energy density and potential energy density, respectively. Here G_α, $\mathbf{c}_\alpha$ and c_i^α represent for any phase α the Gibbs energy function, molar concentration vector and individual concentrations of any component (i = Fe, C, Ni, Cr) respectively.

The Allen–Cahn type evolution equation for the phase α i.e., ϕ_α is derived from the grand-potential functional as shown in Eq. (6). The evolution equation for the chemical potential vector $\boldsymbol{\mu}$ consists of a parameter μ_i for each component (i = Fe, C, Ni, Cr) and is given in Eq. (7). Ψ_α is the grand-potential of the phase α. For details on the derivation and the associated discussion, the reader is referred to [28,35].

$$\tau\epsilon\frac{\partial\phi_\alpha}{\partial t} = \underbrace{-\epsilon\left(\frac{\partial a(\boldsymbol{\phi},\nabla\boldsymbol{\phi})}{\partial\phi_\alpha} - \nabla\cdot\frac{\partial a(\boldsymbol{\phi},\nabla\boldsymbol{\phi})}{\partial\nabla\phi_\alpha}\right) - \frac{1}{\epsilon}\frac{\partial\omega(\boldsymbol{\phi})}{\partial\phi_\alpha} - \frac{\partial\psi(\boldsymbol{\phi},\boldsymbol{\mu},T)}{\partial\phi_\alpha}}_{:=rhs_\alpha} - \underbrace{\frac{1}{N}\sum_{\beta=1}^{N}(rhs_\beta)}_{:=LagrangeMultiplier}, \tag{6}$$

$$\frac{\partial\boldsymbol{\mu}}{\partial t} = \left[\sum_{\alpha=1}^{N} h_\alpha(\boldsymbol{\phi})\left(\frac{\partial c_\alpha(T,\boldsymbol{\mu})}{\partial\mu}\right)\right]^{-1} \left(\nabla\cdot\left(\mathbf{M}(T,\boldsymbol{\mu},\boldsymbol{\phi})\nabla\boldsymbol{\mu} - \mathbf{J}_{at}(T,\boldsymbol{\mu},\boldsymbol{\phi})\right) - \sum_{\alpha=1}^{N}\mathbf{c}_\alpha(T,\boldsymbol{\mu})\frac{\partial h_\alpha(\boldsymbol{\phi})}{\partial t} - \sum_{\alpha=1}^{N} h_\alpha(\boldsymbol{\phi})\left(\frac{\partial c_\alpha(T,\boldsymbol{\mu})}{\partial T}\right)\frac{\partial T}{\partial t}\right). \tag{7}$$

In Eq. (7) the term $\mathbf{J}_{at}(T,\boldsymbol{\mu},\boldsymbol{\phi})$ represents the anti-trapping current which is introduced to account for the solute trapping defect of thin-interface. In thermochemical simulations, the temperature variation is governed by an evolution equation taken from the frozen temperature approximation as

$$\frac{\partial T}{\partial t} = \frac{\partial}{\partial t}\left(T_0 + G\left(x - V_G t\right)\right) = GV_G, \tag{8}$$

where $T_0 = T_s - \Delta T$ and T_s, ΔT, G and V_G are the solidification temperature, the thermal undercooling, the thermal gradient and the thermal gradient velocity. The gradient energy density $a(\boldsymbol{\phi}, \nabla\boldsymbol{\phi})$ with cubic anisotropy $\left(a_c\left(q_n\right)\right)$ is taken as

$$a(\boldsymbol{\phi}, \nabla(\boldsymbol{\phi})) = \sum_{\substack{\alpha,\beta=1\\(\alpha<\beta)}}^{N,N}\gamma_{\alpha\beta}\left(a_c\left(q_n\right)\right)^2|\mathbf{q}_{\alpha\beta}|^2, \tag{9}$$

$$\left(a_c\left(q_n\right)\right) = 1 - \delta_{\alpha\beta}\left(3 - 4\frac{|q_{\alpha\beta}|_4^4}{|q_{\alpha\beta}|^4}\right), \tag{10}$$

where $\mathbf{q}_{\alpha\beta} = \phi_\alpha\nabla\phi_\beta - \phi_\beta\nabla\phi_\alpha$ as normal vector and $q_n = \mathbf{q}_{\alpha\beta}/|\mathbf{q}_{\alpha\beta}|$ as unit vector normal to the interface. The symbols $\gamma_{\alpha\beta}$ and $\delta_{\alpha\beta}$ represent interfacial energy parameter and the interfacial energy anisotropy strength between the phases α and β respectively. At the interface, a double obstacle potential energy density is used, which is defined as

$$\omega(\boldsymbol{\phi}) = \begin{cases} \frac{16}{\pi^2\epsilon}\sum_{\substack{\alpha,\beta=1\\(\alpha<\beta)}}^{N,N}\gamma_{\alpha\beta}\phi_\alpha\phi_\beta & if\, 0<\phi<1 \\ \infty & \text{else.} \end{cases} \tag{11}$$

The individual concentrations c_i are calculated by inverting the corresponding μ_i according to Eq. (12) and related to the relative mobilities according to Eq. (13).

$$\mathbf{c}_i = \sum_{\alpha=1}^{N} c_i^\alpha(\boldsymbol{\mu}, T)\, h_\alpha(\phi), \tag{12}$$

$$\frac{\partial\mathbf{c}_i}{\partial t} = \nabla\cdot\sum_{j=1}^{K-1} M_{ij}^\alpha g_\alpha(\phi)\nabla\mu_j, \tag{13}$$

$$M_{ij}^\alpha = D_{ij}^\alpha\frac{\partial\mathbf{c}_i^\alpha(\boldsymbol{\mu}, T)}{\partial\mu_i}. \tag{14}$$

Here, $i, j = 1, 2, 3, \ldots, K$ denotes any component in the system for a total number of K components. M_{ij}^α and D_{ij}^α given in Eq. (14) represent a second-order tensor for the interfacial mobilities and diffusivities between phase pairs respectively. Here mobilities are interpolated between different phases in the system using an interpolation function

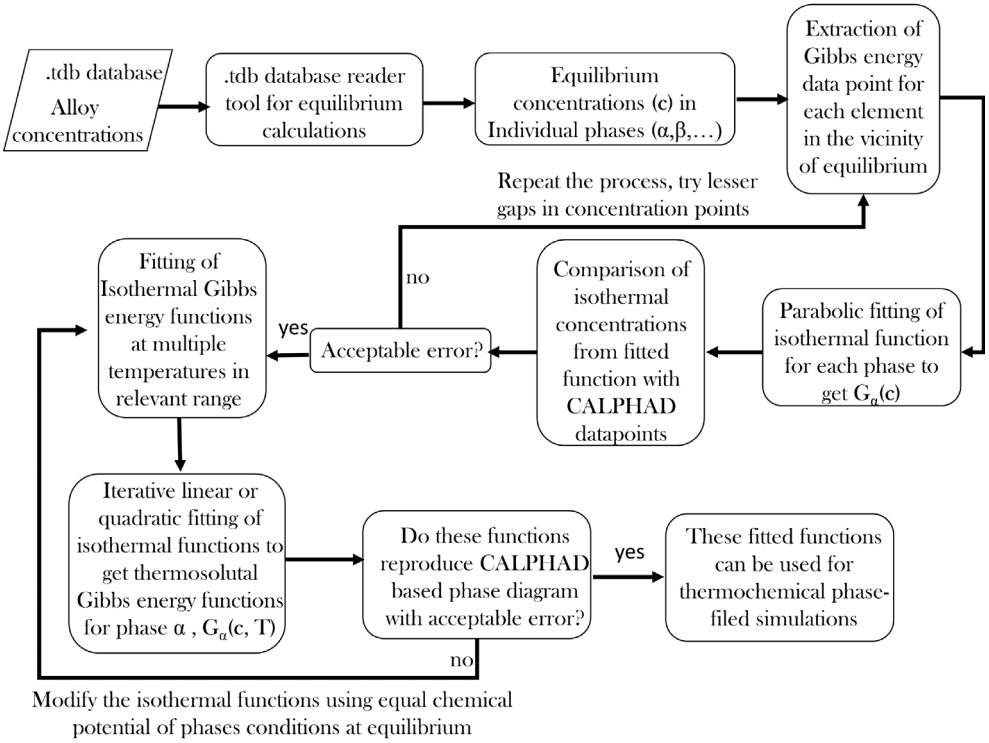

Fig. 2. Flow of activities in the process of fitting Gibbs energy functions for a quaternary alloy from the complex Gibbs energy formulation in CALPHAD database.

i.e. $g_\alpha(\phi)$, which is a different function from $h(\boldsymbol{\phi}_\alpha)$. Off-diagonal mobilities i.e., $M^\alpha_{ij}, \forall i \neq j$ are ignored during the simulation study to minimise the computational complexity of this quaternary system. Therefore, $D^\alpha_{ij}, \forall i = j$ values (i.e., on the diagonal) are used at the input of simulations.

2.2. Gibbs energy fitting for quaternary alloy

The pre-processing step for quantitative phase-field simulations involves getting parabolic Gibbs energy functions from the complex Gibbs energy formulation of the CALPHAD database. For this purpose, the parabolic fitting technique has been extended to a quaternary system, and the process is explained step-wise in the flowchart in Fig. 2. The CALPHAD database by Liu et al. [34] for four components i.e., Fe–C–Cr–Ni is used. The alloy composition of carbon, chromium, nickel, and iron are taken to be 0.092 , 20.281 , 7.586 , and 72.040 at % respectively.

In the first step the equilibrium concentrations of each phase in the two-phase region i.e., (1730 K<T<1749 K) shown in Fig. 1 (B) are calculated using any CALPHAD data reader software (for this study Thermo-Calc [33] is used). In the next step, these concentrations are used to find the local equilibrium concentrations for each element in the vicinity of global equilibrium in each phase. For this purpose, some suitable concentration steps (generally 100–1000) are considered in each direction for each element. In doing so it has to be ensured that the data points are enough to describe the behaviour of concentration-dependent Gibbs energy as well as one has to stay in the vicinity of the equilibrium point for that phase. For elements that are in low concentration in the alloy such as carbon this process can be challenging because the concentration steps cannot be chosen below zero. For this purpose, smaller step size relative to the previously found equilibrium concentrations are chosen for each phase. The step size and number of steps need to be chosen small enough to avoid negative concentrations and large enough to represent the parabolic behaviour near the equilibrium point.

The next step is the isothermal Gibbs energy fitting from the individual concentrations saved in the last step. This will give Gibbs energy functions in the form $G_\alpha(c_i)$ as shown:

$$G_\alpha(c_i) = \sum_{i=1}^{K} A_{\alpha,i} \cdot c_i^2 + \sum_{i=1}^{K} B_{\alpha,i} \cdot c_i + C_\alpha, \quad \alpha = \delta - Fe, Liq., \; i = C, Cr, Ni, Fe, \tag{15}$$

where $A_{\alpha,i}$, $B_{\alpha,i}$ and C_α represent the coefficients of the fitted parabolic function in an isothermal setting. When fitting an isothermal function, ensure that the predicted Gibbs energy values at a single temperature should correspond to the local equilibrium suggested by the CALPHAD database with an acceptable error. The analysis of the relative error in this process was performed for several isothermal functions. The maximum deviation from the CALPHAD values for both the δ − Fe phase and the *Liq* phase is only 0.05% and 0.013% respectively. With this negligible error, the next step for thermosolutal fitting of isothermal functions in the desired temperature range is performed. By linear or quadratic interpolation among various isothermal cases, a thermally continuous representation of the Gibbs energy behaviour throughout the intended temperature range is obtained. In this process, the coefficients of the polynomial for the isothermal functions are made temperature-dependent to get parabolic thermosolutal Gibbs energy functions. The generalised form of these functions for any number of phases and components (represented by the generic symbols α and i respectively) in any alloy system is given as

$$G_\alpha(c_i, T) = \sum_{i=1}^{K} A_{\alpha,i}(T) \cdot c_i^2 + \sum_{i=1}^{K} B_{\alpha,i}(T) \cdot c_i + C_\alpha(T), \quad \alpha = \delta - Fe, Liq., \; i = C, Cr, Ni, Fe, \tag{16}$$

where $A_{\alpha,i}(T)$, $B_{\alpha,i}(T)$ and $C_\alpha(T)$ represent the coefficients of the fitted thermosolutal function. K, c_i, and T stand for the total number of components, their concentrations, and the temperature respectively. The aim is to get the phase diagram from these fitted functions and compare it with the phase diagram from CALPHAD, as shown in Fig. 3 (A-D). There are several challenges associated with this task to capture the complex thermodynamic interaction of all the four components

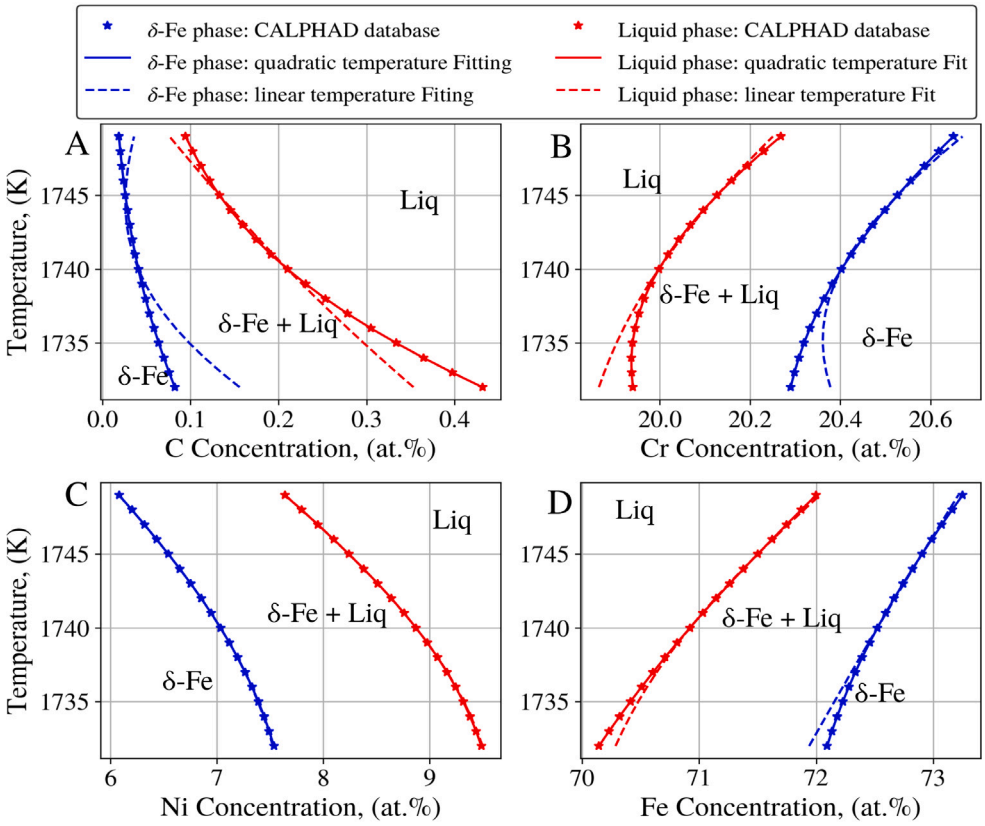

Fig. 3. Comparative pseudo-binary phase diagrams for carbon, chromium, nickel and iron from A to D respectively, showing a comparison of the fitted thermosolutal functions with the CALPHAD database. All the plots show linear and quadratic temperature fitting results for liquidus and solidus. The quadratic fit is adopted in this study due to its low deviation from the CALPHAD database.

along with other state variables.

- As per Gibbs phase rule, the degrees of freedom (F) for a quaternary alloy is four i.e., composition variables, which interplay to define the equilibrium between δ – Fe and *Liq* at any point in 4D space. The solution is to ensure that the error involved is negligible at each isothermal fitting step and cannot potentially become substantial during further processing for thermosolutal fitting.
- The second challenge is the lack of possibility to graphical represent the system in 4D to visualise and verify the chemical potential equality at the equilibrium points even at discrete temperature values. The solution is the mathematical representation of the equality of chemical potentials at equilibrium by extending the criteria as shown in Eq. (17).
- The third challenge is the limited temperature range in which the thermosolutal functions are fitted but in LBW process the 2-phases window can persist longer compared with the predictions by the equilibrium CALPHAD database. For this reason a prediction of thermodynamic behaviour of metastable phases at lower temperature is required. The fitted thermosolutal Gibbs energy functions are capable to predict the approximated extrapolated behaviour at lower temperatures well with reasonable accuracy.

Firstly, the generated thermosolutal functions are compared with CALPHAD database and if there is still considerable difference and the fitted functions do not satisfy standard CALPHAD data, then the modification loop is applied. It is initially described by [26] for simpler binary and ternary systems. For quaternary alloy systems the modification loop is extended in the present work given as

$$\begin{aligned} G_{Liq}|_{C^{eq}_{Liq},Cr^{eq}_{Liq},Ni^{eq}_{Liq}} &= G_{\delta-\mathrm{Fe}}|_{C^{eq}_{\delta-\mathrm{Fe}},Cr^{eq}_{\delta-\mathrm{Fe}},Ni^{eq}_{\delta-\mathrm{Fe}}} \\ &+ \mu^{C}_{\delta-\mathrm{Fe}}|_{C^{eq}_{\delta-\mathrm{Fe}},Cr^{eq}_{\delta-\mathrm{Fe}},Ni^{eq}_{\delta-\mathrm{Fe}}} \times (C^{eq}_{\delta-\mathrm{Fe}} - C^{eq}_{Liq}) \\ &+ \mu^{Cr}_{\delta-\mathrm{Fe}}|_{C^{eq}_{\delta-\mathrm{Fe}},Cr^{eq}_{\delta-\mathrm{Fe}},Ni^{eq}_{\delta-\mathrm{Fe}}} \times (Cr^{eq}_{\delta-\mathrm{Fe}} - Cr^{eq}_{Liq}) \\ &+ \mu^{Ni}_{\delta-\mathrm{Fe}}|_{C^{eq}_{\delta-\mathrm{Fe}},Cr^{eq}_{\delta-\mathrm{Fe}},Ni^{eq}_{\delta-\mathrm{Fe}}} \times (Ni^{eq}_{\delta-\mathrm{Fe}} - Ni^{eq}_{Liq}), \end{aligned} \tag{17}$$

where, G_{Liq} and $G_{\delta-\mathrm{Fe}}$ represents the Gibbs energy of phase *Liq* and δ – Fe at their chemical equilibrium states. The $\mu^{C}_{\delta-\mathrm{Fe}}$, $\mu^{Cr}_{\delta-\mathrm{Fe}}$, and $\mu^{Ni}_{\delta-\mathrm{Fe}}$ represents the chemical potential of carbon, chromium and nickel in phase δ – Fe at equilibrium concentrations respectively. This equation takes three elements into account due to the condition that the sum of all concentrations in mole fractions is equal to 1 at any time in the whole domain, i.e. $\sum_i^K c_i = 1$. This modification loop defines only two basic conditions for satisfaction of thermodynamic equilibrium between δ – Fe and *Liq* by ensuring following two conditions:

- The chemical potential of each component is equal across the coexisting phases. This condition is analogous to the common tangent in binary and ternary systems but involves more dimensions.
- In a quaternary system, the concept extends to a common tangent plane that touches the Gibbs energy surfaces of the phases in equilibrium. This plane represents the condition where the chemical potentials of all components are equal across the phases.

In this loop, the first condition of equal chemical potentials is satisfied using the second condition namely the common tangent construction to the Gibbs energy surfaces to ensure equilibrium conditions for all components involved at the intended temperature. For phases δ – Fe

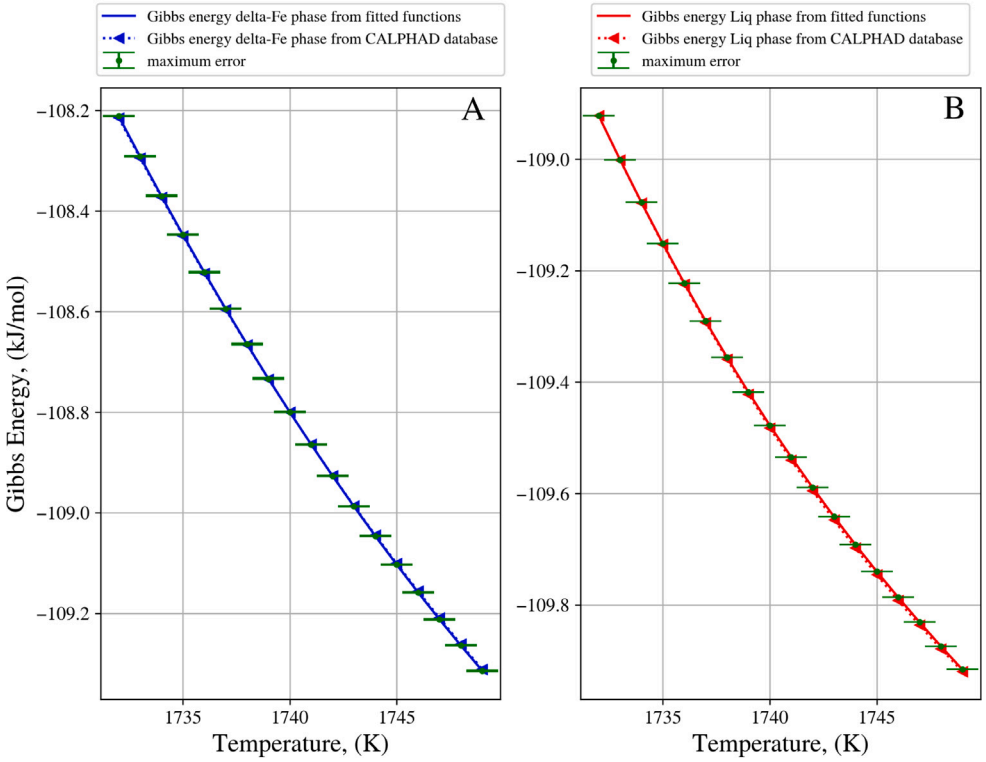

Fig. 4. Comparison of Gibbs energy predicted from parabolic functions with linear and quadratic temperature fitting with CALPHAD database for (A) δ – Fe and (B) *Liq* phases with maximum error less than 1%.

and *Liq* in a quaternary Fe–C–Cr–Ni system, the common tangent plane touches the Gibbs energy surfaces of these phases at specific compositions, indicating equilibrium. This means that the chemical potentials of Fe, C, Cr, and Ni are equal in both phases at equilibrium compositions. In this case, Eq. (17) can only the satisfied when the product of chemical potential of any component i in δ – Fe phase and difference of equilibrium concentrations of i in both phases correspond to the exact difference of Gibbs energy needed to reach the tangent point in *Liq* phase in 4D space. With this strict criterion satisfied the approximated phase diagrams are constructed and compared in Fig. 3. It can be seen that the linear fits shown with the dashed lines do not represent well the solidus and liquidus lines, however, the quadratic fits shown with solid lines matche quite well with the CALPHAD database with accuracy more than 99% in δ – Fe and *Liq* phases. The parabolic Gibbs energy functions with quadratic temperature fitting are shown for δ – Fe and *Liq* phases in Eq. (18) and Eq. (19) respectively. It should be noted that each function is described with three concentration variables instead of four. This is due to the constraint that the sum of all mole fractions must equal one. Consequently, the Fe concentration is replaced with $(1 - C - Cr - Ni)$ in both functions. This modification in the representation of the functions helps to further reduce the computational load during each iteration of the solver loop.

$$
\begin{aligned}
&G_{\delta-\mathrm{Fe}}(C, Cr, Ni, T) = \\
&\quad (-0.996T^2 + 4894.093T - 3022599.155) \cdot C^2 \\
&\quad + (-2.505T^2 + 8657.716T - 7446357.017) \cdot Cr^2 \\
&\quad + (55.937T^2 - 193338.598T + 167156073.417) \cdot Ni^2 + (0.548T^2 \\
&\quad - 1877.632T + 1618543.659) \\
&\quad \cdot (1 - C - Cr - Ni)^2 + (32.132T^2 - 112565.771T + 98564757.836) \cdot C \\
&\quad + (2.205T^2 - 7622.726T \\
&\quad + 6587850.813) \cdot Cr + (-5.739T^2 + 19817.129T - 17137117.347) \cdot Ni \\
&\quad + (-0.532T^2 + 1737.52T - 1526027.948),
\end{aligned}
\tag{18}
$$

$$
\begin{aligned}
&G_{\mathrm{Liq}}(C, Cr, Ni, T) = \\
&\quad (-12.430T^2 + 44343.101T - 37198412.859) \cdot C^2 \\
&\quad + (-3.709T^2 + 12864.117T - 11116189.006) \cdot Cr^2 \\
&\quad + (46.481T^2 - 160714.381T + 138992355.291) \cdot Ni^2 \\
&\quad + (0.539T^2 - 1872.659T + 1634806.634) \\
&\quad \cdot (1 - C - Cr - Ni)^2 + (0.0002T^2 - 17.754T + 7699.232) \cdot C \\
&\quad + (2.032T^2 - 7053.938T + 6120627.595) \cdot Cr \\
&\quad + (-6.064T^2 + 20910.287T - 18056713.142) \cdot Ni \\
&\quad + (-0.363T^2 + 1167.7T - 1044886.325).
\end{aligned}
\tag{19}
$$

The Gibbs energy values predicted with the fitted functions and from the CALPHAD database for δ–Fe and *Liq* phases are compared in Fig. 4 (A) and (B) respectively. The accuracy in the whole temperature range is more than 99% for both phases which makes the functions suitable as a computationally optimised thermodynamic framework to be used in phase-field simulations. According to Eq. (3), the magnitude and direction of the driving force for the entire system can therefore be determined as a grand-potential from the Gibbs energies and their respective derivatives for each phase.

3. Parametric and computational aspects

Before running the phase-field simulations of solidification, the physical values are non-dimensionalised to reduce the finite precision error in the results. The process of non-dimensionalisation involves the systematic elimination of units from the governing equations by introducing appropriate scaling factors. First, the characteristic length and time scales of the system are identified. For instance, the thickness of the solidification front, the diffusive time scale, and the solidification temperature could serve as these characteristic scales, mentioned with l_0, t_0 and T_0 in Table 1. Subsequently, physical parameters such as diffusivities, interfacial energies, temperature gradients, and velocities

Table 1
Suitable non-dimensionalisation scales chosen as the basis for the non-dimensionalisation of the physical parameters.

Non-dimensionalisation scales		
Scale	Value	Units
Length (l_0)	1×10^{-8}	m
Time (t_0)	1×10^{-8}	s
Solidification temperature (T_0)	1749	K
Diffusivity (D_0)	1×10^{-8}	m^2/s
Energy density (E_0)	1×10^{10}	J/m^3
Surface energy (γ_0)	$E_0 \times l_0$	J/m^2
Velocity (v_0)	1	m/s
Molar volume (V_m)	1×10^{-5}	m^3/mol

Table 2
Non-dimensionalised physical parameters used for various simulations.

Non-dimensionalised simulation parameters		
Parameter	Numerical value	Physical value
Δx, Δy	$1 \times l_0$	1×10^{-8} m
Nx, Ny	$2000 \times \Delta x$, $2000 \times \Delta y$	20 µm ×20 µm
Δt	$1 \times t_0$	1×10^{-8} s
Interface thickness parameter (ϵ)	$4 \times \Delta x$	4×10^{-8} m
Initial temperature (T_0)	$0.993529 \times T_0$	1738 K
Thermal gradient (G)	1.8×10^{-7}–1.4×10^{-6}	16 K/mm–134 K/mm
Thermal gradient velocity (V_G)	0.005 - 0.033	0.005 m/s–0.033 m/s
Surface energy ($\gamma_{S/L}$)	0.0025	$0.25\,J/m^2$ [36]
Relaxation coefficient ($\tau_{S/L}$)	0.25	4×10^8 J s/m^4
Solid diffusion coefficient ($D_{\delta-Fe}$)	0.0001	1×10^{-12} m^2/s
Liquid diffusion coefficient (D_{Liq})	0.1	1×10^{-9} m^2/s
Concentration noise amplitude, (ξ_i)	0.00005	–
Cubic anisotropy strength, ($\zeta_{\alpha\beta}$)	0.06	–

are expressed in the form of these basic scales, which are referred to as non-dimensionalisation scales in Table 1. The physical values used as inputs in various simulations for domain space as well as thermal and kinetic conditions are then derived using the basic scales already described in Table 2. The diffusivities of all components in solids and liquids are considered as 10^{-12} m^2/s and 10^{-9} m^2/s respectively as reported in the literature [37].

2D simulations are performed with relative spatial and temporal resolutions, as specified in Table 1. The simulations were carried out with a phase-field solver called PACE3D [38], which has already been used to simulate various phase transformation processes [30,39–44]. All 2D simulations are carried out on the hardware resource 'bwUniCluster 2.0', with 2 × 40 CPU cores with Multiple Processing Interface (MPI). Approximately 24 hours were taken by each simulation to run up to the steady state growth conditions.

The moving window technique is applied in all simulations to reduce computational effort. The moving window technique in the solidification process is a computational strategy designed to reduce the computational expense of simulating large domains by focusing computational resources on a smaller and dynamically changing region of interest. The technique ensures that the critical details of the solidification process, such as dendritic growth and microstructure evolution, are captured accurately within the moving window. The boundary conditions of the window are updated dynamically to reflect the conditions in the larger domain [31,45,46]. In doing so at least a distance of 5 × diffusion length is ensured in front of the solidifying phase in the growth direction, to provide enough liquid to avoid boundary effects. The moving window technique is particularly advantageous for thermochemically coupled simulations, where the efficiency of the calculations is even more important.

4. Results

4.1. Validation of simulation results

To perform a 2D simulation study of the dendritic solidification behaviour of quaternary alloy, the growth parameters need validation. Firstly, it is ensured that the speed of the dendrite tip V_{tip} and the input velocity V_G are the same under steady state growth conditions, as shown in Fig. 5 (A). Similarly in Fig. 5 (B) steady state values of dendrite tip radius R_{tip} are observed stable after about 75 ms. All simulation results in Section 4 are recorded after at least 75 ms to establish steady state values in results. In addition, the steady state values of the dendrite tip radius R_{tip} show an inverse behaviour with V_{tip} in such a way that its value decreases successively with increasing V_{tip}. This behaviour, shown in Fig. 5 (B) corresponds to the fundamental behaviour of dendrites observed experimentally [4,23]. Secondly, according to the classical Ivantsov solution [47] and later developed theory by Trivedi et al. [48], two basic conditions for a dendritic growth problem should be satisfied, i.e. $V_{tip}R_{tip}$ and $V_{tip}R_{tip}^2$ should be constant with respect to each dendrite property. In Fig. 5 (C) and (D) these behaviours against the V_{tip} are displayed. The coefficient of determination (R^2) is above 0.98 for both $V_{tip}R_{tip}$ and $V_{tip}R_{tip}^2$, which represents good agreement with the theoretical models of dendritic growth theory [48]. The minor variations of $V_{tip}R_{tip}$ from the mean value in Fig. 5 (C) should be attributed to the local variation of thermal and chemical driving forces which increases with increasing solidification front velocity [49]. With the validated parameters, 2D simulations are performed to investigate different domains in the mushy zone adjacent to the weld pool boundary or liquidus to show the different solidification morphology depending on the local thermal conditions. Two important factors play a role in defining the local thermal conditions. Firstly, the further away from the centre line of the weld pool, the higher the value of the G measured normal to the weld pool boundary as shown in Fig. 6. This is obvious because the same heat is dissipated in relatively fewer spatial units near the fusion line, which is also justified by the shape of the mushy zone, which is thin near the fusion line, compared to the centre line shown in Fig. 6. The growing solid is always directed perpendicular to the weld pool boundary; therefore, the dendrite tip velocity V_{tip} is always equal to a projection of the laser beam velocity (V_{LB}) as $V_G = V_{tip} = V_{LB} \cdot cos(\alpha)$ [50],schematically presented in Fig. 6. It is important to note here that the solidification front velocity is considered equal to the V_G in all simulations because all the results are presented at steady

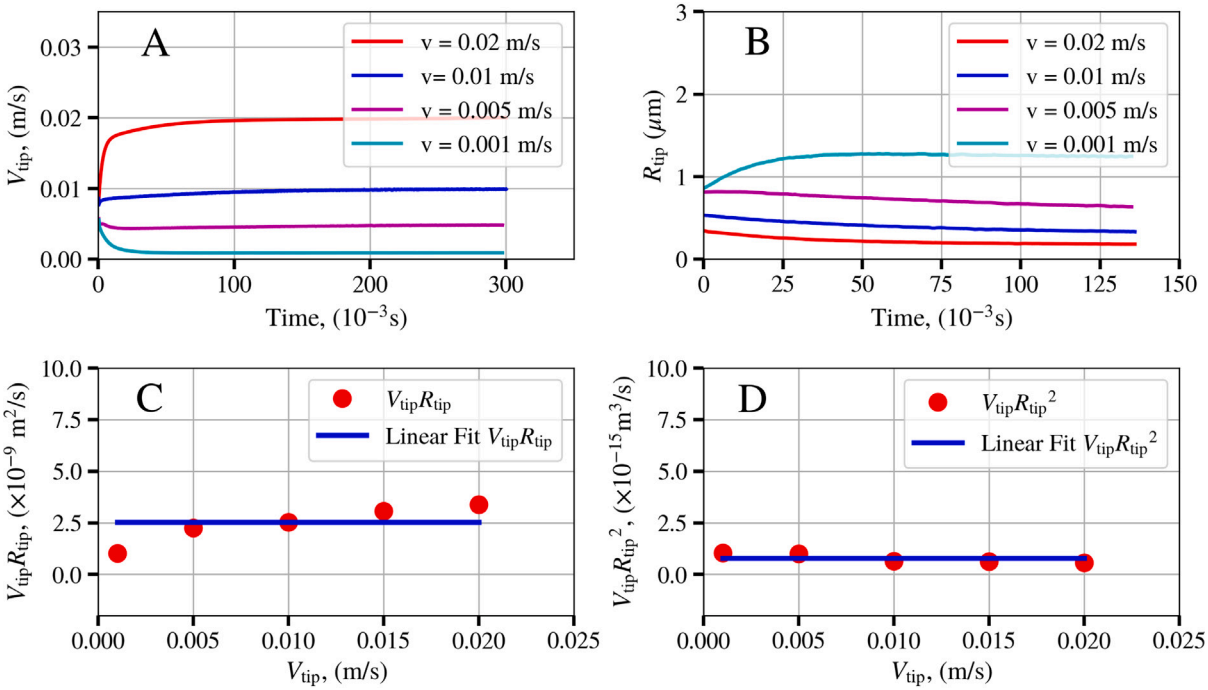

Fig. 5. V_{tip}(A) and R_{tip} (B) of growing dendrites as a function of the time to reach the steady state for different input solidification front velocities. The subplots (C) and (D) show the variation of the velocity with the radius and the linear nature of $V_{tip} \times R_{tip}$ and $V_{tip} \times R_{tip}^2$ for varying V_{tip} respectively.

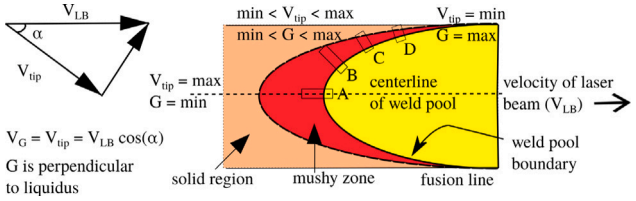

Fig. 6. Local thermal conditions along the weld pool boundary, V_{tip} is always at an angle α with the laser beam velocity V_{LB} i.e., maximum at the centreline of weld and minimum along the fusion line. Conversely G is minimum at the centreline of weld pool and maximum at the fusion line. In between these extremes growth direction is always perpendicular to the weld pool boundary.

state conditions. The angle α increases from 0 to 90 degrees moving from centre line to the fusion line and changes the value of V_{tip} from maximum to minimum, G from minimum to maximum and the cooling rate is calculated as a product of V_{tip} and G.

Four domains are schematically defined at the weld pool boundary on one side of the centre line as A, B, C and D, with decreasing values of V_{tip} as 33 , 20 , 10 , and 5 mm/s respectively. Three values of increasing G are considered along these domains from A-D as 16 , 67 and 134 K/mm respectively. The domain size is selected 20 × 20 μm^2 i.e., large enough to avoid the effect of boundaries on primary dendrite arm spacing (PDAS). At the same time the diffused interface thickness parameter is taken 40 nm to ensure the resolution capable enough to converge the R_{tip} at higher V_{tip} values. The coordinates of the domains are chosen in such a way that the growth is always perpendicular to the isotherm and the front is regarded as a straight line, as the radius of curvature of the isotherm is very large in relation to the size of the dendrite. The simulation results in Fig. 7 show the different morphologies of the growing δ – Fe in the *Liq*, which are decisive for determining the subsequent behaviour of the material and are discussed in detail in the following section.

4.2. Effect of G and V_{tip} on the microstructure evolution

Simulations with a decreasing value of V_{tip}, from 33 to 5 mm/s, are illustrated from top to bottom in Fig. 7 while from left to right, the increasing values of G in K/mm is displayed. The V_{tip} and G are selected in such a way that the effect of growth rates can be observed on morphology evolution. The results are shown at about physical time of 120 ms when the steady state conditions of growth are achieved i.e., the V_{tip} reaches almost the value of the input velocity as verified in Fig. 8 (A). An important factor is the width of the interdendritic region, which is dependent on V_{tip}. It is observed that as the V_{tip} increases for same G, a decrease in PDAS is observed as shown in Fig. 7 (A1, B1, C1, and D1). Conversely, when the G increases with the same V_{tip}, an increase in the number of dendrite per unit length perpendicular to the growth direction is observed as shown in Fig. 7 (A1–A3). Since the local thermal conditions mainly determine the morphology of the solidifying material [51], it is observed that the morphology follows the pattern selection as cellular → columnar-dendritic, when the velocity is increased as shown in Fig. 7 (D2-A2). This is in accordance with the experimentally observed morphology by Hunt et al. [52]. The appearance of the secondary dendrites is observed in the regions where lower values of G and higher values of V_{tip} are considered. The secondary dendrite arms (SDA) compete for space and available solute. Those with more favourable orientations and positions tend to survive. The microstructure becomes more interesting because the critical local thermal conditions allow the dendrites to grow perpendicular to growth direction. This interaction ultimately contributes to interdendritic liquid being trapped in smaller residual liquid pockets. It is observed in Fig. 7 that the fluctuations on the solid/liquid interface are mostly on the higher V_{tip}. For instance, at 33 mm/s going from higher to lower G (from A3 to A1) the probability of the secondary dendrite seems to increase. It is important to note that thermal conditions with lower G and higher V_{tip} correspond to the region adjacent to the centreline of the weld pool during solidification as shown in Fig. 6. The complex morphology of dendrites with SDA is associated directly with V_{tip} and inversely with G. These SDAs increase the time for completion of local solidification which contributes in

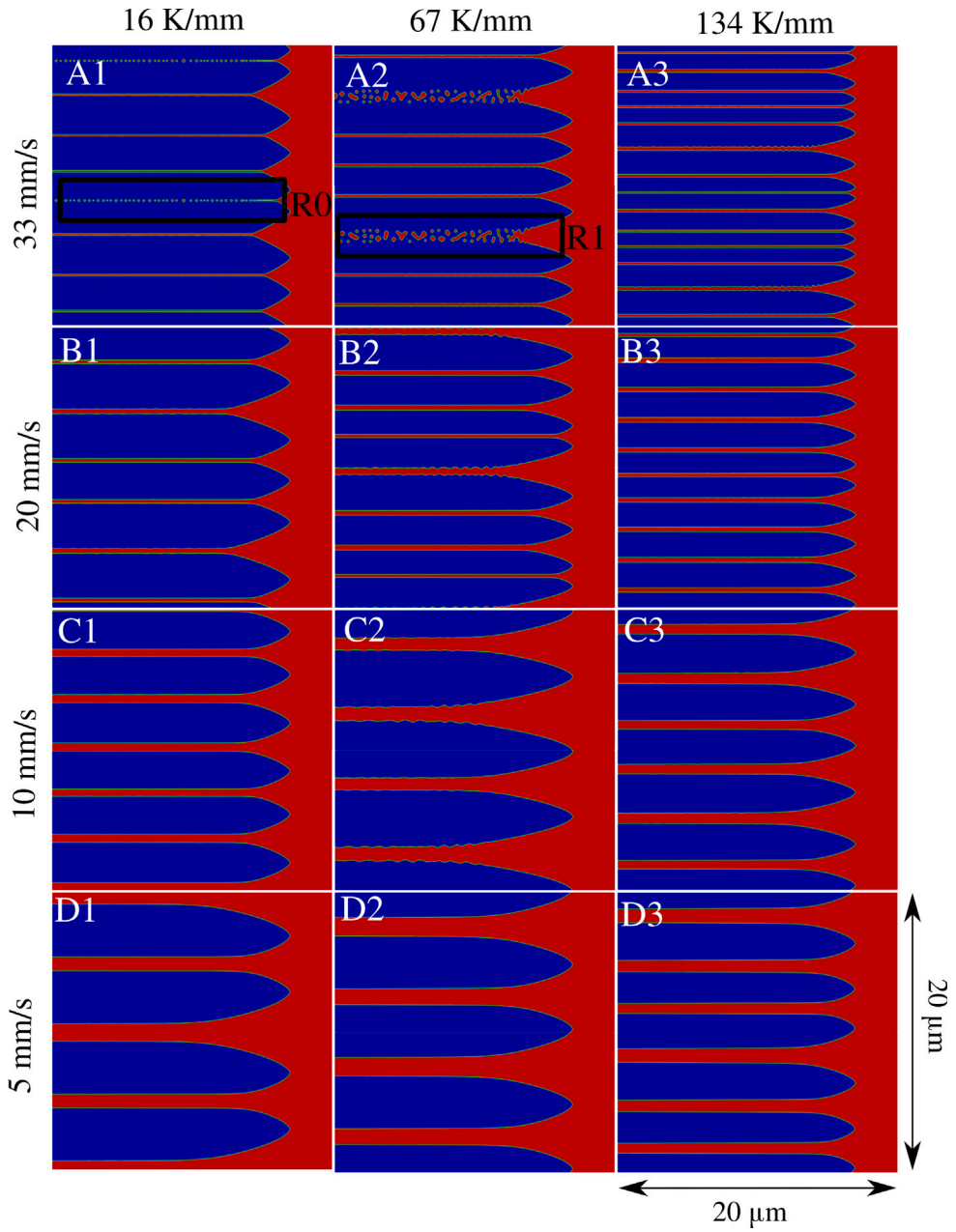

Fig. 7. Effect of G and V_{tip} on the growth pattern of $\delta-$Fe during solidification. The figures A1–A3, B1–B3, C1–C3, and D1–D3 show the effect of increasing G from left to right for V_{tip} value of 33, 20, 10 and 5 mm/s respectively.

delaying the solidification of residual liquid films or pockets as shown in Fig. 7 (A1 and A2) with rectangle R0 and R1.

The relationship between V_{tip} and R_{tip} is crucial in dendritic solidification, as it significantly influences the final microstructure and, consequently, the material properties. This interdependence determines key features such as PDAS and secondary dendrite arm spacing (SDAS), which in turn affect the mechanical and physical characteristics of the solidified alloy. In the current study R_{tip} is observed to be decreasing with the increasing V_{tip}. This relationship is in agreement with the published fundamental literature by Trivedi et al. [48] on dendritic growth given as,

$$R_{tip} \propto \frac{1}{\sqrt{V_{tip}}},$$

shown in Fig. 8 (B). Similarly, PDAS is also inversly related to V_{tip} as depicted in in Fig. 8 (C). This relationship is often expressed as power law equations where PDAS is proportional to V_{tip} raised to a negative exponent often -0.25 as discussed under Fig. 12.

4.3. Effect of microsegregation

It is important to elucidate the microsegregation behaviour of key alloying elements within the mushy zone, namely carbon, chromium and nickel, and correlate their distribution patterns with the underlying solidification kinetics and process parameters. The simulation results show the intricate microsegregation patterns of the alloying elements within the dendritic arms. As the dendritic arms grow and compete for solutes, different segregation profiles develop along the arms, representing enrichment and depletion zones of alloying elements as depicted in Fig. 9. This phenomenon can be attributed to solute partitioning between the liquid and solid phases, driven by the local solidification front curvature and thermal undercooling, which in turn is an effect due to V_{tip}. It can be seen in Fig. 9 for any element that the

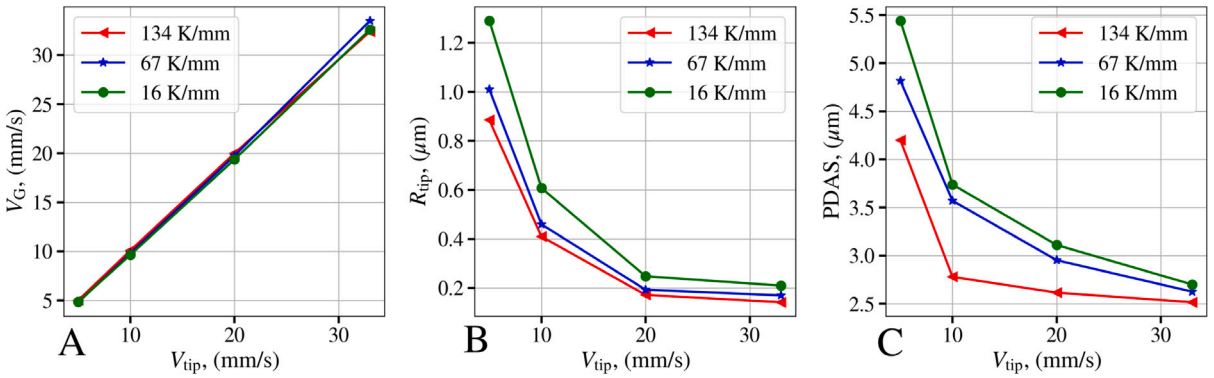

Fig. 8. Relationship of V_{tip}, R_{tip} and PDAS in the simulation study. (A) shows that all the results are presented after V_{tip} approached V_G to ensure the steady state growth conditions. (B) and (C) represent the inverse relation of V_{tip} with R_{tip} and PDAS respectively.

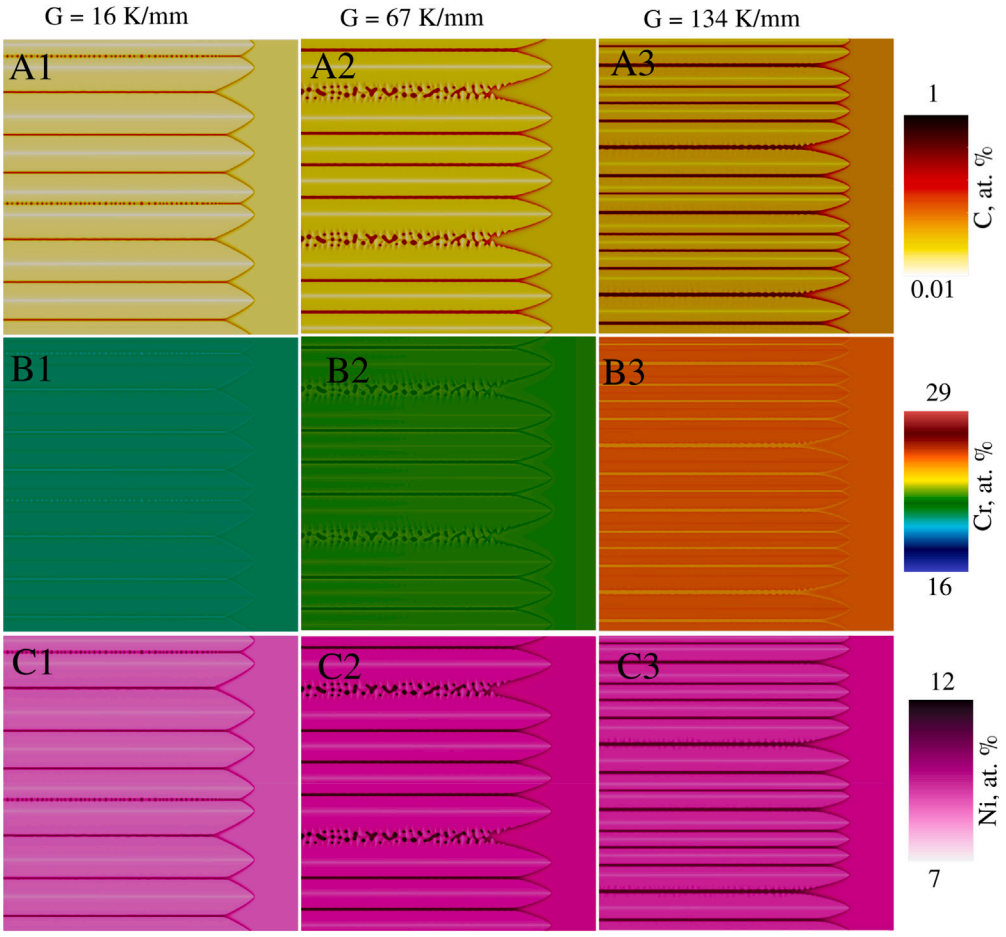

Fig. 9. Component segregation behaviour in quaternary alloy during dendritic solidification at 33 mm/s for (A1-A3) carbon, (B1-B3) chromium and (C1-C3) nickel with G increasing from left to right.

dendrite experiences more undercooling as the velocity increases and thus, in the projected phase diagram, the concentration in both phases increases. This is due to increased growth rate and in agreement with the experimental observations [53].

The influence of solute mobility and diffusivity further determines the extent of segregation. Carbon diffuses into the δ – Fe phase in a limited amount due to its partition coefficient $K_c = 0.19$ being less than unity. As there is not enough time to reach perfect equilibrium conditions, δ – Fe absorbs more solute i.e., 0.08 at % of the available 0.092 at %. Carbon is rejected substantially by growing solid around the dendrite tip. A similar trend is observed for nickel which is also considered to participate in limited amounts in δ – Fe formation due to its partitioning coefficient $K_{Ni} = 0.796$ (i.e., less than unity). The segregation behaviour of the elements observed is in quite well agreement with phase-field simulation conducted for similar alloys and under similar cooling rates by Hariharan et al. and Gao et al. [54,55]. Warren and Boettinger also highlighted the similar segregation patterns of solute with different solid phase diffusivities [56]. As the dendrite further grows, the interdendritic region becomes carbon and nickel rich and the colour contrast represents this behaviour in Fig. 9 (A1-A3) and (C1-C3). Conversely, the chromium concentration is lower in the interdendritic region due to its partition coefficient $K_{Cr} = 1.02$

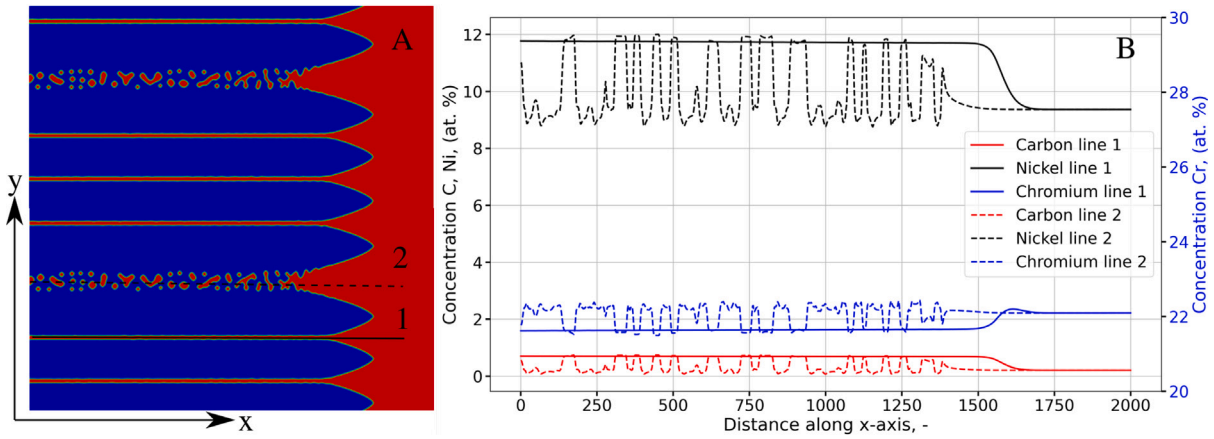

Fig. 10. Microsegregation behaviour of alloying elements: (A) evolved morphology, (B) line plots of the concentrations along the lines 1 and 2 marked in (A) for carbon, chromium, and nickel, respectively. Different microsegregation behaviour of alloying elements in plain liquid channel and trapped liquid pockets is observed.

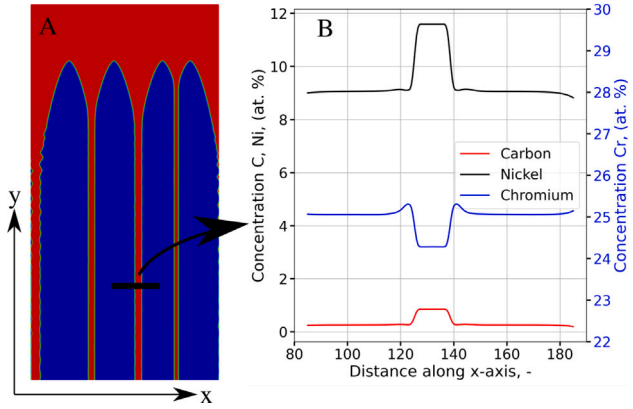

Fig. 11. Microsegregation behaviour of alloying elements: (A) evolve microstructure showing $\delta-$Fe dendrite (blue) and *Liq* phase (red). (B) line plots of the concentrations along the horizontal line in (A) for carbon, chromium, and nickel. Interdendritic liquid is chromium deficient while rich in carbon and nickel.

slightly higher than unity. The segregation behaviour of chromium is shown with light colour in the interdendritic region in Fig. 9 (B1-B3) unlike the carbon and nickel. Concentration plot is shown with the help of line scan in Fig. 10 and Fig. 11 where carbon and nickel are observed concentrated in the interdendritic region, pushed by the growing dendrite interface. Chromium is a δ – Fe former; therefore, it is used by the growing solid, hence has a low concentration in the interdendritic region.

In case of SDA appearance, carbon and nickel are rejected by the growing solid and are trapped in between the primary arms, giving rise to the carbon-rich residual liquid pockets. The long interdendritic liquid channels in Fig. 10 (B), which are in contact with the bulk liquid, have a possibility to exchange solute and therefore produce a uniform solute profile parallel to the growth direction indicated with line 1 in Fig. 10 (A). The line plots for carbon and nickel in Fig. 10 (B) visualise non-uniform concentrations along line 2, where Sharp concentration jumps are seen at the S/L interface represented by a dashed line in Fig. 10 (B).

5. Discussion

The dendritic solidification morphology evolution during LBW is sensitive to the local thermal conditions i.e., G and V_{tip}. One of the most important influencing factors for determining the quality of the resulting weld is PDAS. PDAS is a key microstructural feature that determines the overall solidification structure which in turn is strongly responsible for the mechanical properties of the LBW products. It directly influences the distribution of solute, secondary phases, and defects within the solidified microstructure [57]. The results of simulations, as depicted in Fig. 7, demonstrate the significant influence of the V_{tip} and G on the morphology evolution during dendritic solidification. Systematically varied V_{tip} from 33 to 5 mm/s show the effects under different G values from 16 K/mm to 134 K/mm. A critical observation is the relationship between V_{tip} and the PDAS. As V_{tip} increases for a constant G, there is a noticeable decrease in PDAS, as illustrated in Fig. 7 (A1, B1, and C1). This inverse relationship of PDAS with V_{tip} is illustrated in Fig. 8 (C). Similarly, an inverse relationship with R_{tip} with V_{tip} is also observed as depicted in Fig. 8 (B). This inverse relationship aligns with established theories that faster growth rates result in finer dendritic structures [53]. The simulation results are compared with the PDAS relationship from the analytical work of Hunt et al. [58] in Fig. 12. It is evident that for every case of G, the slop of the $G^{-0.5}V_{tip}{}^{-0.25}$ from simulation results align reasonably with the slop of relationship predicted by the Hunt et al. This means that the scaling of PDAS with the growth rate is reliable in the simulation results. The comparison indicates a fixed offset in every case of G values. The complex thermodynamic interactions in quaternary alloy may influence stability criteria of the dendrites and may change the PDAS. For instance, the growth competition of dendrites in the presence of rejected solutes i.e., carbon and nickel in constitutionally supercooled liquid may affect the PDAS.

As can be observed in the morphological evolution in Fig. 7, dendrites at higher velocity and low G form SDA and after mutual interaction trap residual liquid causing delayed solidification due to local change in concentration. The trapped liquid pockets exhibit strong jumps in concentrations at the S/L interface and limit the further solute exchange with the bulk liquid as in Fig. 10 (B). The volume change of these regions upon solidification is observed experimentally [6] to result in high local strains. On the other hand, continuous liquid film exhibits a homogeneous change in local concentration parallel to the growth direction. The presence of the liquid film may act as longitudinal weak plane if it exists in the incompletely solidified mushy zone unsolidified before the thermal contraction of adjacent solid starts. This effect leads to the formation of pores at the solid–liquid interface, once the solid network is formed at centreline of weld resulting into a defective solidification process. These phenomena are reported by experimentalists as the cause of the difference in mechanical behaviour

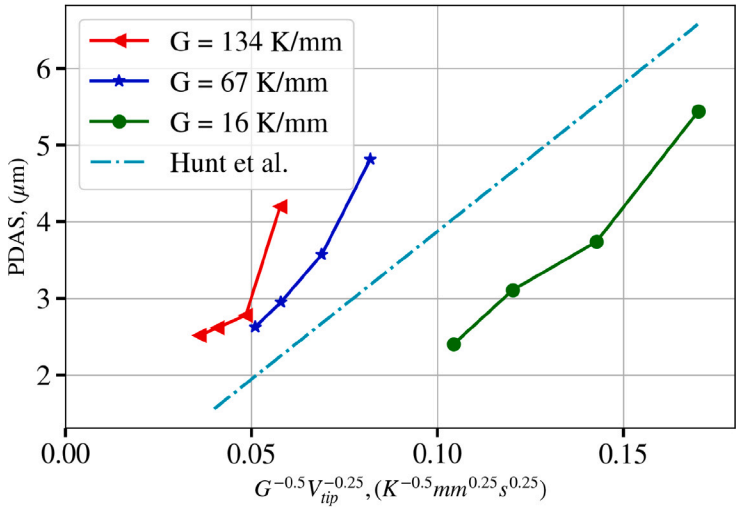

Fig. 12. Quantitative comparison of present study with Hunt's relation between $G^{-0.5}V_{tip}{}^{-0.25}$ and PDAS.

of adjacent phases [59,60].

The microsegregation effects are closely linked to the dendritic morphology. Dendrite tip undercooling induces localised strong solute gradients in faster cooling rates, causing solute atoms to preferentially accumulate on the liquid side, in the vicinity of the dendrite tips, as in the case of carbon and nickel [61]. The formation of secondary arms, driven by competitive growth, leads to further partitioning of alloying elements. The complex interplay between dendritic growth kinetics, solute diffusion and capillary effects is central to shaping the observed microsegregation profiles [62]. The simulation outcomes substantiate that dendritic morphology acts as a crucial mediator for the extent and distribution of components within the mushy zone. The microsegregation patterns show a strong dependence on the local thermal conditions and consequently on the global welding process parameters such as heat input and the speed of laser welding head. Elevated cooling rates tend to amplify the segregation effects by accelerating solute partitioning, leading to more pronounced segregation. Variations in the welding speed change the solidification kinetics, which at higher speeds leads to entrapment of solute-rich/deficient liquid in the dendritic arms. Consequently, higher welding speeds result in higher concentration gradients, due to a shortened solute enrichment time as observed in Fig. 7. These morphological aspects have a strong correlation with the micro segregation behaviour of solutes and consequently with the phenomenon of solute trapping. For this purpose considerations of non-equilibrium solidification for extreme local thermal conditions i.e., V_{tip} dependent partition coefficient will be used in the further simulation study.

6. Conclusion

This study provides an insight into the dendritic morphology evolution and microsegregation effects observed during the solidification of the quaternary X5CrNi18-10 alloy, using phase-field simulations. For this purpose thermodynamic functions are derived from the CALPHAD database. The simulations show the complicated interplay between the dendritic morphology, the solute segregation and the process parameters, which together determine the resulting microstructure. With respect to the modelling and simulation results the following brief conclusions can be drawn:

- The parabolic fitting method of the Gibbs energy functions from the CALPHAD database for a multiphase quaternary alloy (i.e., Fe–C–Cr–Ni) is successfully applied. The maximum error observed in the reconstructed phase diagrams and Gibbs energy functions is less than 0.3%. This work will serve as a basis for further numerical investigations of such alloys of great industrial importance with computational efficiency of 10 times as compared with CALPHAD direct coupling.
- The validation of the simulation results with the dendritic theory of Trivedi et al. with R^2 more than 0.98 shows reliability of the study.
- At lower V_{tip} (i.e., at 5 or 10mm/s), irrespective of the G values the cellular microstructure is observed with absolutely no SDA. Conversely, columnar dendrites are observed with SDAs at higher V_{tip}, especially at lower values of G (i.e., at 33 mm/s and 67 K/mm).
- The simulation results follow the slope of analytical PDAS $G^{-0.5}$ $V_{tip}{}^{-0.25}$ relationship reported by Hunt et al. with a fix offset in the values which is attributed to multi-component interactions, which needs further investigation.
- The study of effect of the local thermal conditions in the weld pool shows that along the centreline the dendrites grow SDA which can entrap the liquid in the form of pockets or long thin films.
- Pronounced microsegregation near the interface of the δ – Fe and residual liquid makes this region most vulnerable to mechanical defects such as voids, due to the local chemical inhomogeneity. It can increase the likelihood of local dissociation at the microscale, which can pose a risk of failure at the last stage of solidification as microcracks.

In view of these observation and findings, it is concluded that presented approach to thermodynamically model the quaternary alloy for quantitative phase-field simulations is suitable for dendritic solidification microstructure evolution study under LBW conditions. There exists a complex correlation of local thermal conditions with the microstructure evolution and microsegregation of alloying elements which is decisive for the quality of weld.

CRediT authorship contribution statement

Muhammad Umar: Writing – review & editing, Writing – original draft, Visualization, Validation, Software, Methodology, Investigation, Formal analysis, Data curation, Conceptualization. **Marco Seiz:** Writing – review & editing, Writing – original draft, Validation, Software, Investigation, Formal analysis, Data curation. **Michael Kellner:** Visualization, Software, Investigation, Conceptualization. **Britta Nestler:** Writing – review & editing, Supervision, Resources, Project administration, Funding acquisition. **Daniel Schneider:** Writing – review

& editing, Supervision, Project administration, Investigation, Funding acquisition, Conceptualization.

Declaration of competing interest

The authors declare that they have no known competing financial interests or personal relationships that could have appeared to influence the work reported in this paper.

Acknowledgements

We gratefully acknowledge the financial support of the German Research Foundation (DFG) in the framework of project no. 434946896 within the research unit FOR5134, (TP-6) "Erstarrungsrisse beim Laserstrahlschweißen: Hochleistungsrechnen für Hochleistungsprozesse - Mikrostruktursimulation der Erstarrung in der Schweißnaht". The financial support of the German Research Foundation (DFG), under grant number NE 822/31-1 (Gottfried Wilhelm Leibniz Prize) is acknowledged. Furthermore, scientific discussions are provided through the programme "MSE", no. 43.31.01 of the Helmholtz association. This work was performed on the bwUniCluster computing resource, which is funded by the Ministry of Science, Research and the Arts of Baden-Württemberg and the universities of Baden-Württemberg, as part of the bwHPC programme. Technical support by Henrik Hierl and fruitful discussions with Paul Wilhelm Hoffrogge, Ahmed Elmogharzy, Sumanth Nani Enugala and Kaveh Noubary Dargahi are also thankfully acknowledged.

Data availability

Data will be made available on request.

References

[1] B. Chalmers, Principles of Solidification, Wiley, New York, 1964.
[2] M.C. Flemings, Solidification processing, Metall. Trans. 5 (10) (1974) 2121–2134.
[3] W. Kurz, D. Fisher, Fundamentals of Solidification, Trans Tech Publications Ltd, Aedermannsdorf, 1986.
[4] M.E. Glicksman, Principles of Solidification: an Introduction to Modern Casting and Crystal Growth Concepts, Springer Science & Business Media, Berlin [U.A.], 2010.
[5] D. Manitsas, J. Andersson, Hot cracking mechanisms in welding metallurgy: A review of theoretical approaches, MATEC Web of Conf. 188 (2018) 03018, http://dx.doi.org/10.1051/matecconf/201818803018.
[6] M. Norouzian, M.A. Elahi, P. Plapper, A review: Suppression of the solidification cracks in the laser welding process by controlling the grain structure and chemical compositions, J. Adv. Join. Process. 7 (2023) 100139, http://dx.doi.org/10.1016/j.jajp.2023.100139.
[7] M. Hunkel, Segregations in steels during heat treatment–A consideration along the process chain, HTM J. Heat Treat. Mater. 76 (2) (2021) 79–104, http://dx.doi.org/10.1515/htm-2020-0006.
[8] J.A. Brooks, A.W. Thompson, Microstructural development and solidification cracking susceptibility of austenitic stainless steel welds, Int. Mater. Rev. 36 (1) (1991) 16–44, http://dx.doi.org/10.1179/imr.1991.36.1.16.
[9] S. Wang, R. Sekerka, Computation of the dendritic operating state at large supercoolings by the phase field model, Phys. Rev. E 53 (1996) 3760–3776, http://dx.doi.org/10.1103/PhysRevE.53.3760, URL http://link.aps.org/doi/10.1103/PhysRevE.53.3760.
[10] L. Wang, N. Wang, N. Provatas, Liquid channel segregation and morphology and their relation with hot cracking susceptibility during columnar growth in binary alloys, Acta Mater. 126 (2017) 302–312, http://dx.doi.org/10.1016/j.actamat.2016.11.058, cited By 26.
[11] M. Umar, F. Qayyum, M.U. Farooq, L.A. Khan, S. Guk, U. Prahl, Investigating the effect of cementite particle size and distribution on local stress and strain evolution in spheroidized medium carbon steels using crystal plasticity-based numerical simulations, Steel Res. Int. 92 (3) (2021) 2000407, http://dx.doi.org/10.1002/srin.202000407.
[12] F. Qayyum, M. Umar, V. Elagin, M. Kirschner, F. Hoffmann, S. Guk, U. Prahl, Influence of non-metallic inclusions on local deformation and damage behavior of modified 16MnCrS5 steel, Crystals 12 (2) (2022) 281, http://dx.doi.org/10.3390/cryst12020281.
[13] M. Umar, F. Qayyum, M.U. Farooq, S. Guk, U. Prahl, Qualitative investigation of damage initiation at meso-scale in spheroidized C45EC steels by using crystal plasticity-based numerical simulations, J. Compos. Sci. 5 (8) (2021) 222, http://dx.doi.org/10.3390/jcs5080222.
[14] P. Jiang, S. Geng, X. Shao, G. Mi, C. Wang, H. Wu, C. Han, S. Gao, Fine grains reduce cracking susceptibility during solidification: Insights from phase-field simulations, JOM 71 (9) (2019) 3223–3229, http://dx.doi.org/10.1007/s11837-019-03342-w, cited By 0.
[15] H. Diepers, D. Ma, I. Steinbach, History effects during the selection of primary dendrite spacing. comparison of phase-field simulations with experimental observations, J. Cryst. Growth 237–239, Part 1 (2002) 149–153, http://dx.doi.org/10.1016/S0022-0248(01)01932-7, URL http://www.sciencedirect.com/science/article/pii/S0022024801019327, The thirteenth international conference on Crystal Growth in conjunction with the eleventh international conference on Vapor Growth and Epitaxy.
[16] P. Galenko, S. Reutzel, D. Herlach, S. Fries, I. Steinbach, M. Apel, Dendritic solidification in undercooled Ni–Zr–Al melts: Experiments and modeling, Acta Mater. 57 (20) (2009) 6166–6175, http://dx.doi.org/10.1016/j.actamat.2009.08.043, URL http://www.sciencedirect.com/science/article/pii/S1359645409005540.
[17] W. Boettinger, J. Warren, The phase-field method: simulation of alloy dendritic solidification during recalescence, Metall. Mater. Trans. A 27 (3) (1996) 657–669, http://dx.doi.org/10.1007/BF02648953.
[18] B. Böttger, J. Eiken, M. Ohno, G. Klaus, M. Fehlbier, R. Schmid-Fetzer, I. Steinbach, A. Bührig-Polaczek, Controlling microstructure in magnesium alloys: A combined thermodynamic, experimental and simulation approach, Adv. Eng. Mater. 8 (4) (2006) 241–247, http://dx.doi.org/10.1002/adem.200500241.
[19] R. Kobayashi, Modeling and numerical simulations of dendritic crystal growth, Physica D 63 (3) (1993) 410–423, http://dx.doi.org/10.1016/0167-2789(93)90120-P, URL http://www.sciencedirect.com/science/article/pii/016727899390120P.
[20] J. Warren, W. Boettinger, Prediction of dendritic growth and microsegregation patterns in a binary alloy using the phase-field method, Acta Metall. Mater. 43 (2) (1995) 689–703, http://dx.doi.org/10.1016/0956-7151(94)00285-P, URL http://www.sciencedirect.com/science/article/pii/095671519400285P.
[21] A. Monas, O. Shchyglo, S.-J. Kim, C.D. Yim, D. Höche, I. Steinbach, Divorced eutectic solidification of Mg-Al alloys, JOM 67 (8) (2015) 1805–1811, http://dx.doi.org/10.1007/s11837-015-1418-4.
[22] X. Wang, P. Liu, Y. Ji, Y. Liu, M. Horstemeyer, L. Chen, Investigation on microsegregation of IN718 alloy during additive manufacturing via integrated phase-field and finite-element modeling, J. Mater. Eng. Perform. 28 (2) (2019) 657–665, http://dx.doi.org/10.1007/s11665-018-3620-3, cited By 11.
[23] J. Lipton, M. Glicksman, W. Kurz, Dendritic growth into undercooled alloy metals, Mater. Sci. Eng. 65 (1) (1984) 57–63, http://dx.doi.org/10.1016/0025-5416(84)90199-X.
[24] J. Lipton, W. Kurz, R. Trivedi, Rapid dendrite growth in undercooled alloys, Acta Metall. 35 (4) (1987) 957–964, http://dx.doi.org/10.1016/0001-6160(87)90174-X.
[25] C. Liu, A. Davis, J. Fellowes, P.B. Prangnell, D. Raabe, P. Shanthraj, CALPHAD-informed phase-field model for two-sublattice phases based on chemical potentials: η-phase precipitation in Al-Zn-Mg-Cu alloys, Acta Mater. 226 (2022) 117602, http://dx.doi.org/10.1016/j.actamat.2021.117602.
[26] K. Dargahi Noubary, M. Kellner, J. Hötzer, M. Seiz, H.J. Seifert, B. Nestler, Data workflow to incorporate thermodynamic energies from Calphad databases into grand-potential-based phase-field models, J. Mater. Sci. 56 (2021) 11932–11952, http://dx.doi.org/10.1007/s10853-021-06033-7.
[27] A. Choudhury, B. Nestler, Grand-potential formulation for multicomponent phase transformations combined with thin-interface asymptotics of the double-obstacle potential, Phys. Rev. E 85 (2 Pt 1) (2012) 021602, http://dx.doi.org/10.1103/PhysRevE.85.021602.
[28] M. Plapp, Unified derivation of phase-field models for alloy solidification from a grand-potential functional, Phys. Rev. E 84 (2011) 031601, http://dx.doi.org/10.1103/PhysRevE.84.031601, URL https://link.aps.org/doi/10.1103/PhysRevE.84.031601.
[29] M. Kellner, Modellierung Mehrkomponentiger Materialsysteme Für Die Phasenfeldmethode Und Analyse Der Simulierten Mikrostrukturen (Ph.D. thesis), Karlsruhe, Karlsruher Institut für Technologie (KIT), 2020, http://dx.doi.org/10.5445/IR/1000119330.
[30] A. Choudhury, M. Kellner, B. Nestler, A method for coupling the phase-field model based on a grand-potential formalism to thermodynamic databases, Curr. Opin. Solid State Mater. Sci. 19 (5) (2015) 287–300, http://dx.doi.org/10.1016/j.cossms.2015.03.003, URL http://www.sciencedirect.com/science/article/pii/S135902861500025X.
[31] J. Hötzer, M. Jainta, P. Steinmetz, B. Nestler, A. Dennstedt, A. Genau, M. Bauer, H. Köstler, U. Rüde, Large scale phase-field simulations of directional ternary eutectic solidification, Acta Mater. 93 (2015) 194–204, http://dx.doi.org/10.1016/j.actamat.2015.03.051, URL http://www.sciencedirect.com/science/article/pii/S135964541500227X.
[32] M. Kellner, I. Sprenger, P. Steinmetz, J. Hötzer, B. Nestler, M. Heilmaier, Phase-field simulation of the microstructure evolution in the eutectic NiAl-34Cr system, Comput. Mater. Sci. 128 (2017) 379–387, http://dx.doi.org/10.1016/j.commatsci.2016.11.049.

[33] J.-O. Andersson, T. Helander, L. Höglund, P. Shi, B. Sundman, Thermo-calc & DICTRA, computational tools for materials science, CALPHAD 26 (2) (2002) 273–312, http://dx.doi.org/10.1016/S0364-5916(02)00037-8.

[34] W. Liu, C. Chen, Y. Tang, Q. Long, S. Wei, G. Zhang, F. Mao, Q. Jiang, T. Zhang, M. Liu, Thermodynamic evaluation and investigation of solidification microstructure in the Fe–Cr–Ni–C system, CALPHAD 69 (2020) 101763, http://dx.doi.org/10.1016/j.calphad.2020.101763.

[35] A. Choudhury, B. Nestler, Grand-potential formulation for multicomponent phase transformations combined with thin-interface asymptotics of the double-obstacle potential, Phys. Rev. E 85 (2) (2012) 021602, http://dx.doi.org/10.1103/PhysRevE.85.021602.

[36] Y. Yang, S. Luo, P. Wang, W. Wang, M. Zhu, Multiphase field modeling of dendritic solidification of low-carbon steel with peritectic phase transition, Metall. Mater. Trans. B 52 (6) (2021) 3708–3719, http://dx.doi.org/10.1007/s11663-021-02297-1.

[37] K. Karayagiz, L. Johnson, R. Seede, V. Attari, B. Zhang, X. Huang, S. Ghosh, T. Duong, I. Karaman, A. Elwany, et al., Finite interface dissipation phase field modeling of Ni–Nb under additive manufacturing conditions, Acta Mater. 185 (2020) 320–339, http://dx.doi.org/10.1016/j.actamat.2019.11.057.

[38] J. Hötzer, A. Reiter, H. Hierl, P. Steinmetz, M. Selzer, B. Nestler, The parallel multi-physics phase-field framework PACE3D, J. Comput. Sci. 26 (2018) 1–12, http://dx.doi.org/10.1016/j.jocs.2018.02.011.

[39] E. Schoof, P.G.K. Amos, D. Schneider, B. Nestler, Influence of stress-free transformation strain on the autocatalytic growth of bainite: A multiphase-field analysis, Materialia 9 (2020) 100620, http://dx.doi.org/10.1016/j.mtla.2020.100620, URL http://www.sciencedirect.com/science/article/pii/S2589152920300375.

[40] P.G.K. Amos, E. Schoof, N. Streichan, D. Schneider, B. Nestler, Phase-field analysis of quenching and partitioning in a polycrystalline Fe-C system under constrained-carbon equilibrium condition, Comput. Mater. Sci. 159 (December 2018) (2019) 281–296, http://dx.doi.org/10.1016/j.commatsci.2018.12.023.

[41] O. Tschukin, A. Silberzahn, M. Selzer, P.G.K. Amos, D. Schneider, B. Nestler, Concepts of modeling surface energy anisotropy in phase-field approaches, Geotherm. Energy 5 (1) (2017) 19, http://dx.doi.org/10.1186/s40517-017-0077-9.

[42] D. Schneider, F. Schwab, E. Schoof, A. Reiter, C. Herrmann, M. Selzer, T. Böhlke, B. Nestler, On the stress calculation within phase-field approaches: a model for finite deformations, Comput. Mech. 60 (2) (2017) 203–217, http://dx.doi.org/10.1007/s00466-017-1401-8, URL http://link.springer.com/10.1007/s00466-017-1401-8.

[43] D. Schneider, E. Schoof, O. Tschukin, A. Reiter, C. Herrmann, F. Schwab, M. Selzer, B. Nestler, Small strain multiphase-field model accounting for configurational forces and mechanical jump conditions, Comput. Mech. (2017) 1–18, http://dx.doi.org/10.1007/s00466-017-1458-4, URL http://link.springer.com/10.1007/s00466-017-1458-4.

[44] D. Schneider, O. Tschukin, A. Choudhury, M. Selzer, T. Böhlke, B. Nestler, Phase-field elasticity model based on mechanical jump conditions, Comput. Mech. 55 (5) (2015) 887–901, http://dx.doi.org/10.1007/s00466-015-1141-6.

[45] A. Vondrous, M. Selzer, J. Hötzer, B. Nestler, Parallel computing for phase-field models, Int. J. High Perform. Comput. Appl. 28 (1) (2014) 61–72, http://dx.doi.org/10.1177/1094342013490972.

[46] M. Bauer, J. Hötzer, P. Steinmetz, M. Jainta, M. Berghoff, F. Schornbaum, C. Godenschwager, H. Köstler, B. Nestler, U. Rüde, Massively parallel phase-field simulations for ternary eutectic directional solidification, 2015, CoRR abs/1506.01684, arXiv:1506.01684.

[47] G. Ivantsov, The temperature field around a spherical, cylindrical, or pointed crystal growing in a cooling solution, Dokl. Akad. Nauk SSSR 58 (1947) 567–569.

[48] R. Trivedi, W. Kurz, Dendritic growth, Int. Mater. Rev. 39 (2) (1994) 49–74, http://dx.doi.org/10.1179/imr.1994.39.2.49.

[49] A. Mullis, J. Rosam, P. Jimack, The prediction of tip radius during rapid dendritic growth under coupled thermo-solutal control: What value σ, Trans. Indian Inst. Met. 62 (2009) 309–313, http://dx.doi.org/10.1007/s12666-009-0048-3.

[50] S. Kou, Welding Metallurgy, vol. 431, (no. 446) New Jersey, USA, 2003, pp. 223–225, http://dx.doi.org/10.1002/0471434027.

[51] H. Singer, I. Singer-Loginova, J. Bilgram, G. Amberg, Morphology diagram of thermal dendritic solidification by means of phase-field models in two and three dimensions, J. Cryst. Growth 296 (1) (2006) 58–68, http://dx.doi.org/10.1016/j.jcrysgro.2006.07.033, URL https://www.sciencedirect.com/science/article/pii/S0022024806007469.

[52] J. Hunt, S.-Z. Lu, Numerical modeling of cellular/dendritic array growth: spacing and structure predictions, Metall. Mater. Trans. A 27 (1996) 611–623, http://dx.doi.org/10.1007/BF02648950.

[53] B. Lu, Y. Li, H. Wang, Y. Wang, W. Yu, Z. Wang, G. Xu, Effects of cooling rates on the solidification behavior, microstructural evolution and mechanical properties of Al–Zn–Mg–Cu alloys, J. Mater. Res. Technol. 22 (2023) 2532–2548, http://dx.doi.org/10.1016/j.jmrt.2022.12.082.

[54] V. Hariharan, B. Nithin, L. Ruban Raj, S.K. Makineni, B. Murty, G. Phanikumar, Modeling microsegregation during metal additive manufacturing: Impact of dendrite tip kinetics and finite solute diffusion, Crystals 13 (5) (2023) 842, http://dx.doi.org/10.3390/cryst13050842.

[55] H. Gao, G. Agarwal, M. Amirthalingam, M. Hermans, Hot cracking investigation during laser welding of high-strength steels with multi-scale modelling approach, Sci. Technol. Weld. Join. 23 (4) (2018) 287–294, http://dx.doi.org/10.1080/13621718.2017.1384884.

[56] J.A. Warren, W.J. Boettinger, Prediction of dendritic growth and microsegregation patterns in a binary alloy using the phase-field method, Acta Metall. Mater. 43 (2) (1995) 689–703, http://dx.doi.org/10.1016/0956-7151(94)00285-P.

[57] Z. Jin, X. Kong, L. Ma, J. Dong, X. Li, Prediction of primary dendrite arm spacing of the inconel 718 deposition layer by laser cladding based on a multi-scale simulation, Materials 16 (9) (2023) 3479, http://dx.doi.org/10.3390/ma16093479.

[58] J. Hunt, Cellular and primary dendrite spacings, in: Solidification and Casting of Metals\ Proc. Conf.\, Sheffield, England, July 1977, 1979, pp. 3–9.

[59] P. Yu, K. Thompson, J. McCarthy, S. Kou, Microstructure evolution and solidification cracking in austenitic stainless steel welds, Weld. J 97 (11) (2018) 301–314, http://dx.doi.org/10.29391/2018.97.026.

[60] F. Bodaghi, M. Movahedi, A. Kokabi, Estimation of solidification cracking susceptibility in Al–Si–Cu alloy weld: effects of anisotropic permeability and deformation orientation, J. Mater. Res. Technol. 23 (2023) 2351–2361, http://dx.doi.org/10.1016/j.jmrt.2023.01.138.

[61] X. Shi, S.-C. Duan, W.-S. Yang, H.-J. Guo, J. Guo, Effect of cooling rate on microsegregation during solidification of superalloy INCONEL 718 under slow-cooled conditions, Metall. Mater. Trans. B 49 (2018) 1883–1897, http://dx.doi.org/10.1007/s11663-018-1169-z.

[62] E. Brener, Effects of surface energy and kinetics on the growth of needle-like dendrites, J. Cryst. Growth 99 (1–4) (1990) 165–170, http://dx.doi.org/10.1016/0022-0248(90)90505-F.